3D auxetic cementitious-polymeric composite structure with compressive strain-hardening behavior

Xu, Yading; Šavija, Branko

DOI
10.1016/j.engstruct.2023.116734

Publication date
2023

Document Version
Final published version

Published in
Engineering Structures

Engineering Structures 294 (2023) 116734

Contents lists available at ScienceDirect

Engineering Structures

journal homepage: www.elsevier.com/locate/engstruct

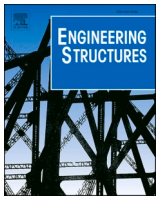

3D auxetic cementitious-polymeric composite structure with compressive strain-hardening behavior

Yading Xu *, Branko Šavija

Microlab, Delft University of Technology, the Netherlands

ARTICLE INFO

Keywords:
Auxetic cementitious composites
3D printing
Mechanical properties
Anisotropy

ABSTRACT

A composite can have properties much better than the components it is made of. This work proposes a three-dimensional auxetic cementitious-polymeric composite structure (3D-ACPC) which incorporates 3D printed polymeric shell with cementitious mortar. Uniaxial compression experiments are performed on the 3D-ACPC to study their quasi-static stress-strain response. Experimental results show that the created composite structure can simultaneously overcome the brittleness of conventional cementitious material and the low compressive strength of 3D printed polymeric cellular shell. Therefore, the 3D-ACPC exhibit compressive strain-hardening behavior ensuring high energy absorption ability. In addition, it is found that structural anisotropy and the shell printing direction have significant impact on the stress-strain response of the 3D-ACPC. Moreover, due to the lightweight cellular structure, the 3D-ACPC shows significantly enhanced specific energy absorption compared to conventional cementitious materials and polymeric cellular materials. To this end, the developed 3D-ACPC has great potential to be used in engineering practice, such as protective structures.

1. Introduction

Auxetic behavior indicates an unique mechanical property: negative Poisson's ratio [1]. This means that, when subjected to vertical compressive load, auxetic structures tend to contract in the transversal direction or vice versa, unlike conventional materials. This allows auxetic structures to endure large deformation, therefore, they can achieve high energy absorption ability [2,3]. In this sense, auxetic structures are of great engineering interest, for example as sacrificial claddings [4–6] which require high energy absorption.

Auxetic structures have attracted increasing research interest in recent years [7–12]. Normally, auxetic behavior is achieved by introducing architected cellular structures, for instance re-entrant structures [13–15], chiral structures [7,16,17], and double arrow structures [8,10,18–20]. One common feature shared by these structures is their highly porous cellular system. As a result, auxetic structures made of a single polymer usually exhibit low compressive resistance due to the porous cellular structure and the low rigidity of polymers. Consequently, their energy absorption capacity is relatively low compared to auxetic structures made of other materials.

Rather than using a single polymeric material to produce auxetic structures, it has been found that creating multi-materials framework-filler composites [20–25] helps to improve energy absorption capacity. Cementitious materials could be an outstanding choice as the filler material. As one of the most used engineering materials, cementitious materials can achieve excellent mechanical properties at very low cost. More importantly, their high stiffness enables them to have great potential to absorb energy when subjected to external load. However, due to the lack of ductility, the deformability of conventional cementitious materials is very low which limits the energy absorption ability at large deformation. Nevertheless, previous studies [26,27] have shown that by adopting polymeric fiber reinforced cementitious materials, the developed auxetic cementitious-polymeric composites can achieve compressive strain-hardening behavior. This allows creating composites with significantly improved energy absorption capacity. Adopting similar approach, cementitious materials could be promising choices to integrate with polymeric auxetic structures, and create composites with excellent energy absorption capacity.

Herein, a novel approach for creating cellular auxetic composite is proposed: using cementitious mortar to enhance compressive strength, while using a polymeric shell to construct auxetic cellular structure and provide ductility. An auxetic cementitious-polymeric composite with three-dimensional cellular structure (3D-ACPC) is first fabricated. Then, the mechanical behavior of the 3D-ACPC is experimentally investigated

* Corresponding author at: Stevinweg 1, 2628CN, Delft, The Netherlands
E-mail address: y.xu-5@tudelft.nl (Y. Xu).

https://doi.org/10.1016/j.engstruct.2023.116734

Available online 9 August 2023

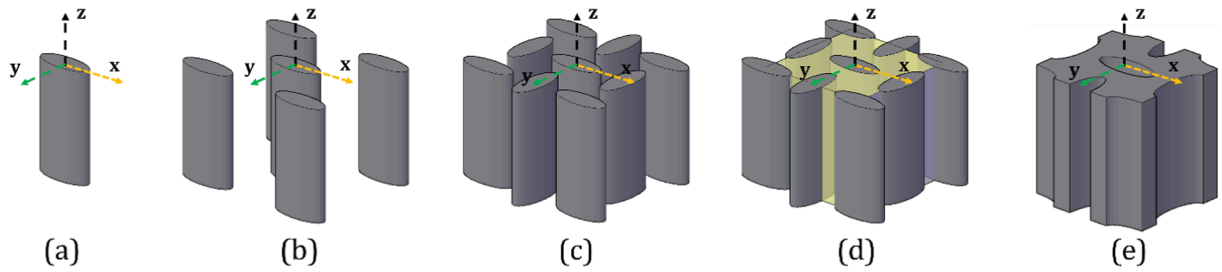

Fig. 1. Schematics of creating the planar auxetic geometry A^{xoy} in the *xoy* plane.

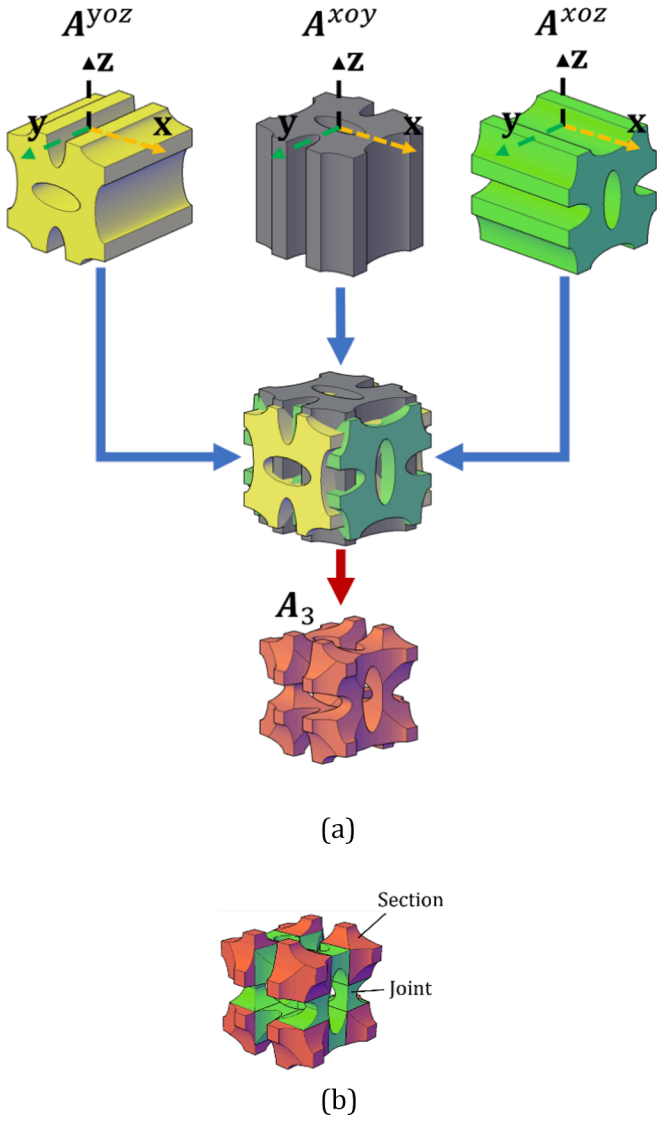

Fig. 2. Schematics of a) creating the 3D auxetic structure, b) definition of the "section" (red regions) and "joint" (green regions). (For interpretation of the references to colour in this figure legend, the reader is referred to the web version of this article.)

under quasi-static compressive load. Specifically, the stress-strain response and energy absorption features of the 3D-ACPC are studied. In addition, the impact of structural anisotropy and shell printing direction on the mechanical properties of the composite is elaborated.

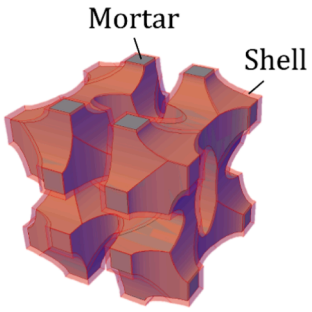

Fig. 3. The 3D auxetic core-shell cementitious composites.

Table 1
Printing parameters used to print the auxetic ABS shell.

Parameters	Configuration
Nozzle diameter (mm)	0.6
Temperature (°C)	260
Layer height (mm)	0.15
Line width (mm)	0.35
Infill density (%)	100
Infill pattern	Lines
Printing speed (mm/s)	45

2. Materials and methods

2.1. Design of the cellular structure

Prior to preparing the specimens, the cellular structure was designed by the following procedures:

In $\mathbb{R}^3$, a set of points: $v_o^{xoy} = (x, y, z)$ satisfying the Eq. (1) was used to describe an elliptical cylinder, as shown in Fig. 1a. In this work, $a = 8$ mm, $b = 20$ mm and $h = 40$ mm was used.

$$(x/a)^2 + (y/b)^2 \leq 1, |z| \leq h \tag{1}$$

where,

x, y, z are the spatial coordinates of the points in the set;
a and b are the minor and major axis of the elliptical cylinder, respectively;
h is the height of the elliptical cylinder.

Then, the elliptical cylinder was transformed in the *xoy* plane to form an array of elliptical cylinders, by the transformation matrix: M_i^{xoy} written in Eq. (2) to Eq. (4), as shown in Fig. 1b.

$$M_i^{xoy} = \begin{pmatrix} E_3 & t_i^{xoy} \\ 0 & 1 \end{pmatrix} \tag{2}$$

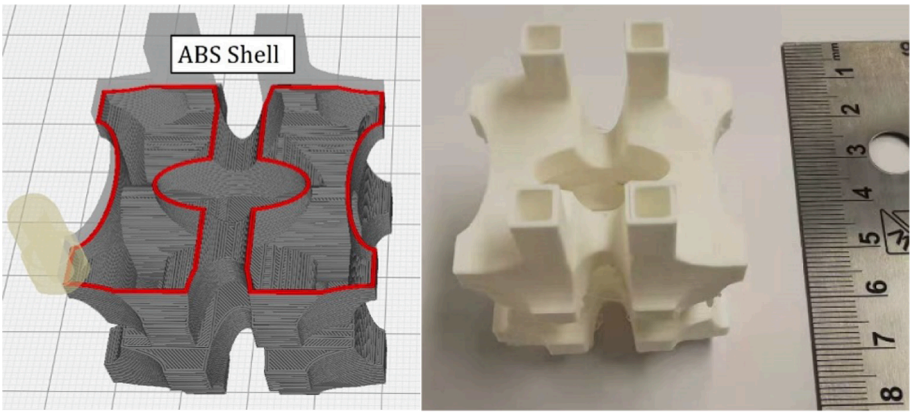

Fig. 4. A) The printing process of the abs shell, b) a printed abs shell.

Table 2
Mixture design of the matrix material (g/l).

CEM I 42.5 N	Fly ash	Sand (0.125–0.250 mm)	Superplasticizer (Glenium 51)	Water	w/b
458	542	458	2	396	0.40

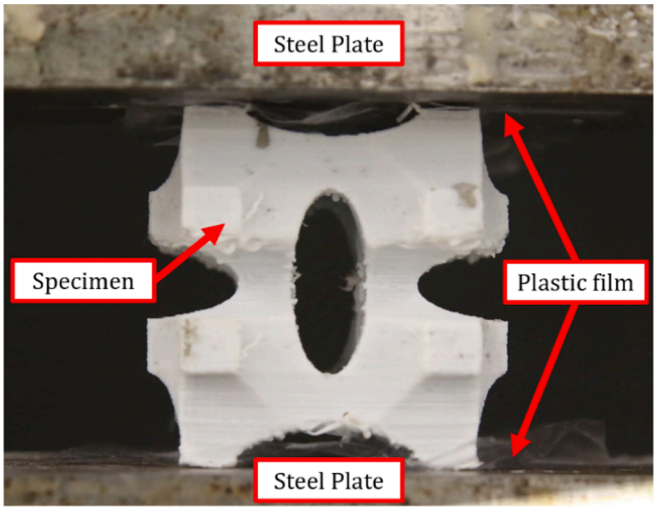

Fig. 5. Experiment set-up for uniaxial compression tests.

$$t_i^{xoy} = \begin{pmatrix} \sin\frac{i\pi}{2} + \cos\frac{i\pi}{2} \\ \sin\frac{i\pi}{2} - \cos\frac{i\pi}{2} \\ 0 \end{pmatrix} * \frac{h}{2}, i \in \{0,1,2,3,4\} \quad (3)$$

$$v_i^{xoy} = M_i^{xoy} \times v_o^{xoy} \quad (4)$$

where,

E_3 is a 3 × 3 unit matrix;
i is an integer determining the number of transformed cylinders;
t_i^{xoy} is the number i th translational transformation vector on the xoy plane;
M_i^{xoy} is the number i th transformation matrix on the xoy plane;

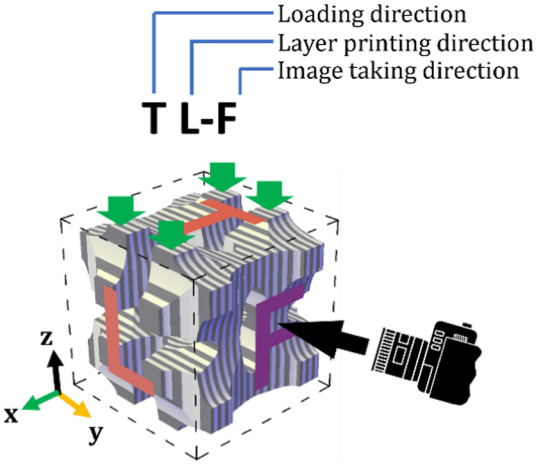

Fig. 6. An example of the notation rule for the tested specimens; it shows this specimen is uniaxial loaded from the top (T) with layers printed from left (L) and pictures taken from front (F); note that the shell was always printed from bottom up, namely the "L" direction was on the printer build plate herein.

v_i^{xoy} is the number i th elliptical cylinders on the xoy plane.

Subsequently, the original elliptical cylinder v_o^{xoy} was rotated along the z axis by the rotation matrix R^{xoy} to create a rotated point set v_R^{xoy}, then, translated by the transformation matrix written by Eq. (7) to Eq. (9), as shown in Fig. 1c.

$$R^{xoy} = \begin{pmatrix} 0 & -1 & 0 \\ 1 & 0 & 0 \\ 0 & 0 & 1 \end{pmatrix} \quad (5)$$

$$v_R^{xoy} = R^{xoy} \times v_o^{xoy} \quad (6)$$

$$N_j^{xoy} = \begin{pmatrix} E_3 & t_j^{xoy} \\ 0 & 1 \end{pmatrix} \quad (7)$$

$$t_j^{xoy} = \begin{pmatrix} sin\frac{i\pi}{2} \\ -cos\frac{i\pi}{2} \\ 0 \end{pmatrix} * \frac{h}{2}, j \in \{1,2,3,4\} \quad (8)$$

$$v_j^{xoy} = N_j^{xoy} \times v_R^{xoy} \quad (9)$$

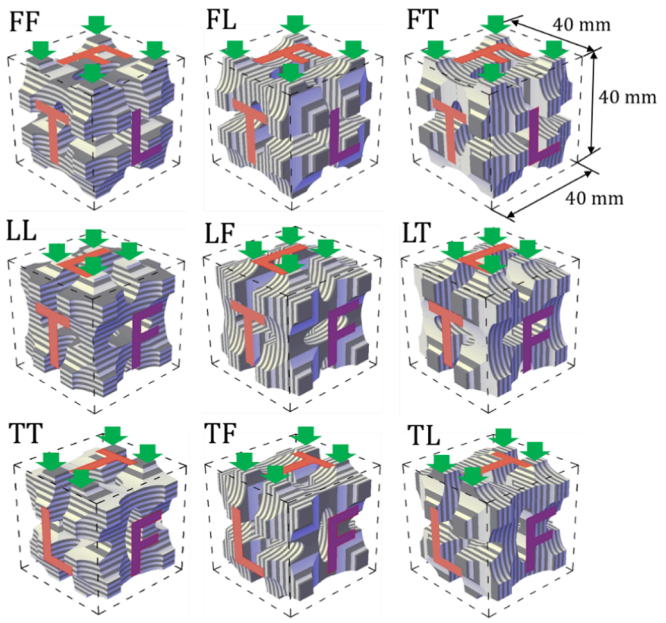

Fig. 7. All printed and tested groups of the designed composite structure, the layered pattern indicating the 3D printing direction is shown; the dimension of all unit cell size is kept the same and indicated.

where,

R^{xoy} is the rotation matrix;
v_R^{xoy} is the rotated point set;
j is an integer determining the number of rotated cylinders;
t_j^{xoy} is the number j th rotational transformation vector on the xoy plane;
N_j^{xoy} is the number j th rotational transformation matrix on the xoy plane;
v_j^{xoy} is the number j th rotated new point set on the xoy plane.

The set of points of all elliptical cylinders on the xoy plane (v^{xoy}) is, therefore, the union of v_i^{xoy} and v_j^{xoy}, and described as:

$$v^{xoy} = v_i^{xoy} \cup v_j^{xoy} \tag{10}$$

Afterwards, the elliptical set was subtracted by a solid cube $\boldsymbol{C}$ (shown in Fig. 1d) which has an edge length of h, to create a planar auxetic geometry similar to [26,27], and it was described by points set $\boldsymbol{A}^{xoy}$, as indicated in Fig. 1e.

The same processes were also performed on the *yoz* and *xoz* plane such that $\boldsymbol{A}^{yoz}$ and $\boldsymbol{A}^{xoz}$ were also obtained. At last, the 3D auxetic structure $\boldsymbol{A}_3$ can be written as the intersection of these planar geometries, namely:

$$\boldsymbol{A}_3 = \boldsymbol{A}^{xoy} \cap \boldsymbol{A}^{yoz} \cap \boldsymbol{A}^{xoz} \tag{11}$$

where,

$\boldsymbol{A}_3$ is the point set of the 3D auxetic structure;
$\boldsymbol{A}^{xoy}$, $\boldsymbol{A}^{yoz}$ and $\boldsymbol{A}^{xoz}$ are the point set of 2D auxetic structure on the xoy, yoz and xoz plane, respectively.

And, the schematics of creating the 3D auxetic structure is shown in Fig. 2a. For convenience, "joint" (coloured in green) and "section" (coloured in red) regions were defined, as shown in (Fig. 2b).

2.2. Specimen preparation

It has been found in previous studies [26–28] that, besides specially designed cellular structures, ductility is necessarily required for cementitious materials to achieve auxeticity and compressive strain-hardening behavior. Therefore, a polymeric material was used as the outer shell of the 3D-ACPC to introduce auxetic structure and ductility, while the cementitious mortar was casted as a filler inside the polymeric shell (shown in Fig. 3).

A commercial 3D printer Ultimaker 2+ was used to print the shell (0.7 mm thickness) of the designed 3D cellular structure. ABS (Acrylonitrile Butadiene Styrene) has been found in our previous work [29,30] to be an efficient reinforcement material for cementitious mixtures. Therefore, ABS was also used in this work as the printing material for the shell. Printing parameters are shown in Table 1. Schematics of printing the ABS shell is shown in Fig. 4a, and a printed ABS shell is shown in Fig. 4b. According to the manufacturer Ultimaker [31], the tensile strength and elongation at break of bulk ABS is 43.6 MPa and 34%, while for the printed ABS is 39.0 MPa and 4.8%, respectively.

It needs to be noted that the designed auxetic structure may have significant anisotropic behavior under compression. This, on one hand, is an intrinsic property of the created 3D auxetic structure; on the other hand, the printing directions of the polymeric shell may introduce additional influences. Therefore, the ABS shell was printed and loaded in different directions to investigate the anisotropic mechanical behavior. A detail explanation of all printed and tested specimens is given in section 2.4.

2.3. Mixing, casting and curing

As complex 3D geometry was used for the shell, high flowability was needed for the cementitious mixture to ensure good casting quality of the specimens. The cementitious mixture proportion is listed in Table 2: a fine-grained mortar with water-to-binder ratio (w/b) of 0.40 was used to cast the 3D-ACPC specimens.

Weighted dry materials were first mixed for 4 min, then water and superplasticizer were added, followed by another 4 min of mixing. Afterwards, the fresh cementitious mixture was loaded into a syringe and intruded into the printed ABS shell, followed by 60 s of vibrating. After casting, all specimens were covered by plastic films and kept under room temperature for 1 day. Afterwards, the specimens were cured in tap water at room temperature until an age of 28 days.

2.4. Mechanical tests

A hydraulic press (INSTRON 8872) was used to perform the uniaxial compression tests. The experimental set-up is shown in Fig. 5, two fixed steel loading plates were used to apply the external compressive load. Two plastic films were placed between the specimen and steel loading plates to reduce friction. A uniaxial downwards displacement was applied by the upper steel plate at a quasi-static rate of 0.01 mm/s until 45% strain of the specimens. Load was recorded by the load cell, and displacement was recorded by the machine stroke. During the tests, a digital camera was placed facing in front of the specimen to take pictures. Afterwards, the pixels number between two pairs of outermost (top/bottom and left/right) edges of the specimen at different strain was counted. The change of pixels number is then used to calculate the Poisson's ratio of the 3D-ACPC.

As indicated before, the loading and the shell printing directions may have an influence on the compressive behavior of the 3D-ACPCs. Therefore, the prepared specimens were categorized into three series according to the loading direction (three directions), and three subdivisions according to the printing direction (three directions). As shown in Fig. 6, the "F", "L" and "T" indicates front, left and top, respectively. In this sense, in total nine types of specimens were tested: FF, FT, FL, LL, LF, LT, TT, TF, TL as shown in Fig. 7. Note that the picture taking direction would not influence the stress-strain response of the specimens and is, therefore, not listed.

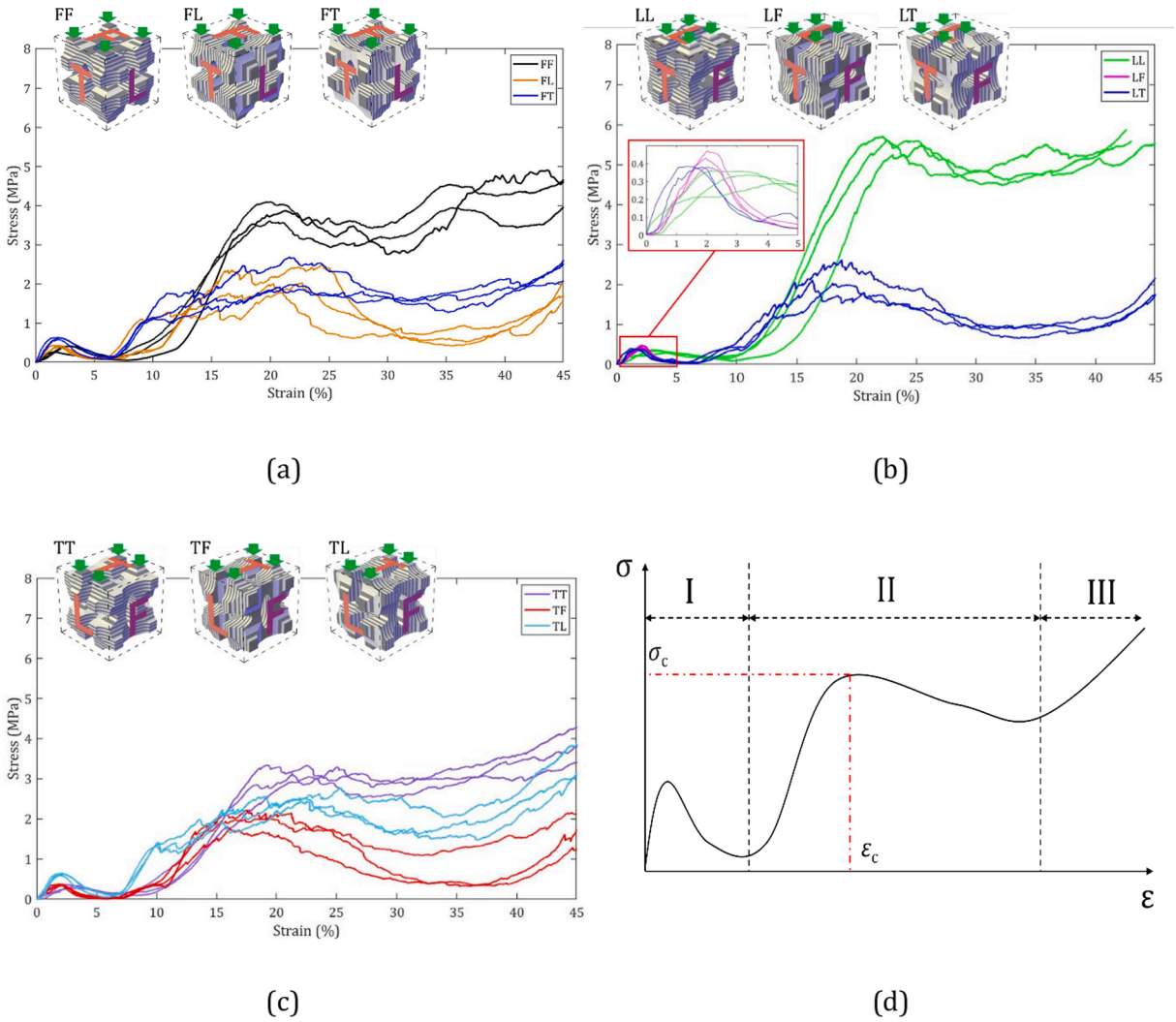

Fig. 8. Stress-strain curves of the 3D-ACPCs loaded from a) the "F" direction, b) the "L" direction and c) the "T" direction; three duplicates were tested for each sample shown in the Fig. 7.

3. Results and discussion

3.1. Stress-strain response

The stress-strain curves of all tested 3D-ACPC are calculated based on the obtained load and displacement data from the INSTRON 8872. The cube within which the unit cells were created was used to calculate the stress and strain. As indicated in Fig. 7, the cross-sectional area is 40 × 40 mm^2, and the specimen height is 40 mm. All obtained stress-strain curves are shown in Fig. 8. It is clearly shown that, as a result of structural anisotropy and varying printing direction, the compressive response of all tested specimens distinctly differs from each other. Except the LF specimen, all other orientations exhibit compressive strain-hardening behavior, namely higher compressive stress is reached after the first peak. The stress-strain curve of the 3D-ACPC can be roughly divided into three consecutive stages (as indicated in Fig. 8d), according to the compression process of the specimens. The authors have observed the same trend in previously developed 2D-ACCCs [26,28], and have been reported to occur in many other types of auxetic materials [13,14,32,33]. The compressive strength, σ_c, of the 3D-ACPC is defined as the highest peak stress excluding stage "III", and the deformability, ε_c, as the strain corresponding to the compressive strength.

In stage "I", the stress-strain curves correspond to the damage and contraction process of the 3D cellular structure. As compressive strain increases, one peak stress is first obtained, followed by a descending branch as seen in Fig. 8a ~ Fig. 8d. Within this stage, the 3D-ACPC exhibit auxetic behavior, triggered by the so-called "crack-initiated-rotation" [26,27] mechanism: cracks initiate at the "joint" regions accompanied by horizontal contraction of the specimen. For instance, Fig. 9 shows the deformation process of the "FF" specimens. At 5% strain, cracks can be clearly seen at the joint regions. The cracked joints act as hinges allowing the sections to rotate alongside compression progresses, as seen in Fig. 9b. As a result, horizontal contraction of these specimens is witnessed, and the 3D-ACPC exhibit a negative Poisson's ratio (see Fig. 10). The data of the measured Poisson's ratio is listed in Table 3.

Within this stage, negative Poisson's ratio is witnessed by the 3D-ACPC. It can be seen from Fig. 10a that the Poisson's ratio of FF decreases with compressive strain. This agrees well with the deformation behavior (Fig. 9a) of the 3D-ACPC in stage "I". It is worth noting that, due to the structural anisotropy, the Poisson's ratio values measured from two observed directions ("L" and "T" for the FF specimen) is different. Similar trend of the Poisson's ratio is also observed on the specimens loaded from the "L" (Fig. 10b) and "T" (Fig. 10c) direction.

The precise strain range of the stages are determined according to the energy absorption efficiency of the 3D-ACPC. Referring to [34], the energy absorption efficiency E is defined as:

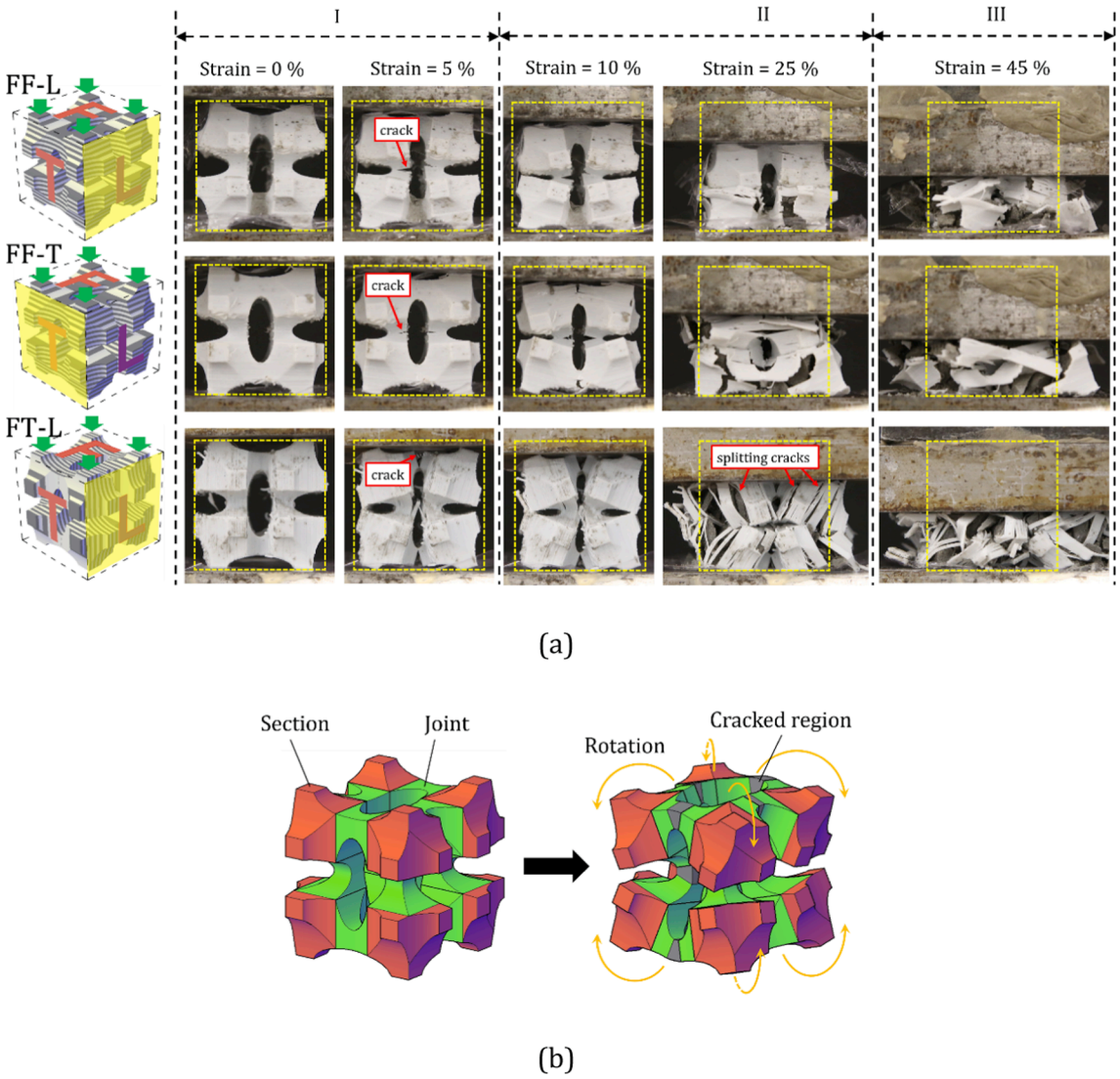

Fig. 9. A) Compression process of the ff specimens, roughly divided in three stages; b) a schematic description of the "crack-initiated-rotation" mechanism.

$$E = \frac{\int_0^{\varepsilon_m} \sigma d\varepsilon}{\sigma_m} \quad (1)$$

where ε_m and σ_m is compressive strain and stress, respectively. In this work, as shown in Fig. 11, two peaks dividing the stress-strain curve to three stages can be found on the energy absorption efficiency curve. The strain ε_I of the first peak indicates the strain limit of stage "I", ε_{II} of the second peak indicates the strain limit of stage "II", after which stage "III" starts. The strain limit is influenced by the structural anisotropy and printing direction as well; results of 3D-ACPC tested from all directions are listed in Table 4.

Stage "II" is the strain-hardening stage. Strain-hardening occurs due to subsequent compacting of the cellular structure after stage "I". It can be seen in Fig. 9 that the sections of the 3D-ACPC starts to get into contact as the strain increases over 10%. Consequently, the stress starts to increase again until the second peak is reached, as shown in the stress-strain curves in Fig. 8a. Correspondingly, though still being negative, the Poisson's ratio observed from both directions also starts to increase as seen in Fig. 10a. Alongside further strain increase, the cellular structure is crushed and eventually crushed to rubble, leading to stress drop after the second peak. The energy absorption ability of the 3D-ACPC is significantly increased in this stage due to the strain-hardening behavior. This sharply differs from some conventional cementitious foams [35–37] which normally show a "plateau" or "platform" stress-strain response in this stage, i.e. no strain-hardening behavior.

Stage "III" is called the densification stage. In this stage, rubble generated in the previous stage is further compacted. During this process, the material fragments are densely pressed which results in sharp stress increase as shown in Fig. 8. A similar phenomenon was also found in other types of auxetic materials [38], and was postulated to exist in conventional concrete as mentioned in a thought experiment [39].

3.2. Compressive strength

While the general trend of the stress-strain response of 3D-ACPC resemble each other, the influence of structural anisotropy and printing direction is critical. A most intuitive observation is the deformation process of the 3D-ACPC. For example, Fig. 9a shows the deformation of FT specimen which is loaded from the "F" direction while the shell was printed from the "T" direction. In stage "I" the FT specimen shows cracking behavior similar to the FF (shown in Fig. 9a). In contrast, in stage "II" multiple splitting cracks can be witnessed on the FT specimen.

The possible reason for such difference is attributed to the influence of printing directions of the ABS shell. As indicated previously, the interface between printed layers of the FT shell is parallel to the loading direction. As well understood by many studies [40–42], due to the weak

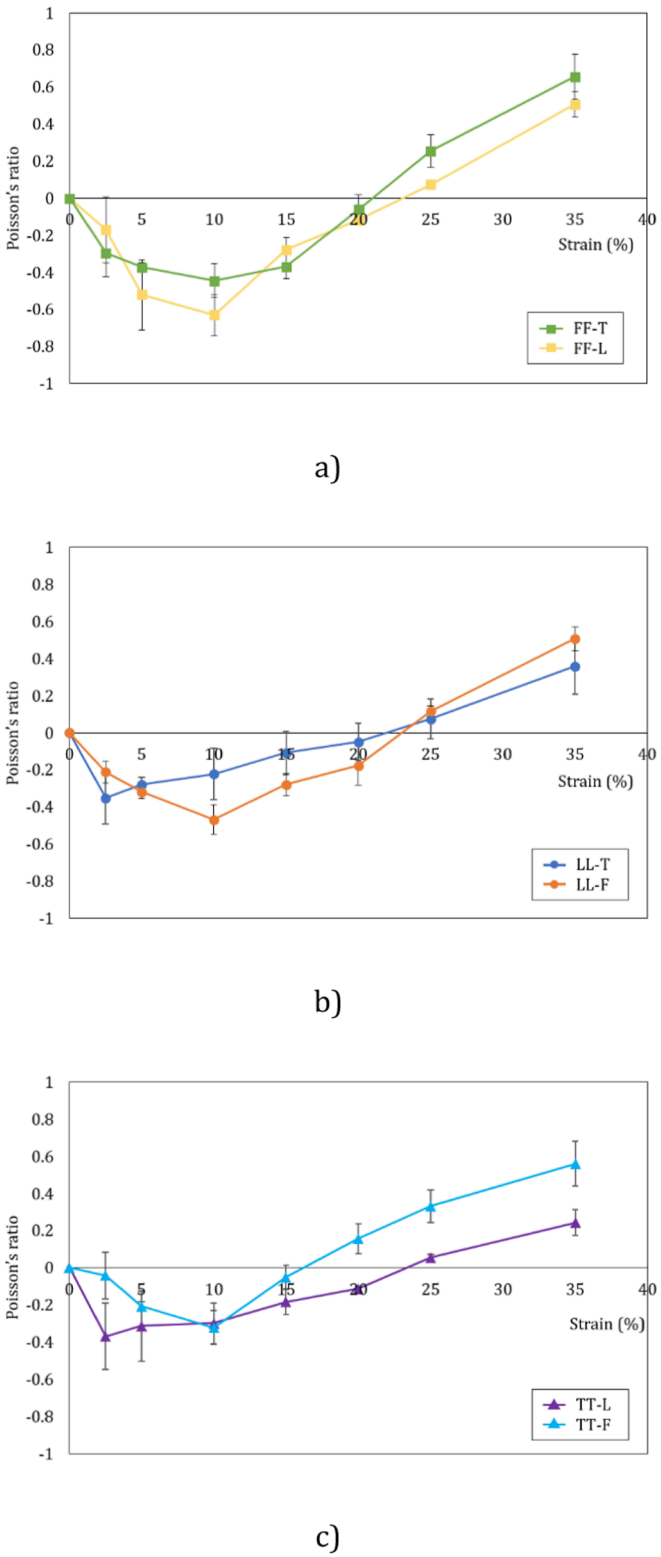

Fig. 10. Poisson's ratio of the a) FF specimen, b) LL specimen and c) TT specimen measured from two observation directions until 35% of strain, standard deviation is indicated;

interface of printed layers, an object exhibits lower compressive strength when the printed interface is parallel to the loading direction than perpendicular to it. As a result, as can be seen in Fig. 12, the compressive strength (defined by the highest peak strength before stage "II") of the FT and FL specimens is 2.2 MPa and 2.1 MPa, respectively. The fact that

Table 3
Possion's ratio of the specimens at different strain, values are rounded to two digits.

Strain (%)	Poisson's ratio					
	FFL	FFT	TTL	TTF	LLT	LLF
0	0	0	0	0	0	0
2.5	−0.17	−0.30	−0.37	−0.04	−0.35	−0.21
5.0	−0.52	−0.37	−0.31	−0.21	−0.28	−0.32
10	−0.63	−0.45	−0.30	−0.32	−0.22	−0.47
15	−0.28	−0.37	−0.18	−0.05	−0.11	−0.28
20	−0.12	−0.06	−0.11	0.16	−0.05	−0.18
25	0.07	0.25	0.06	0.33	0.08	0.12
35	0.51	0.66	0.24	0.56	0.36	0.51

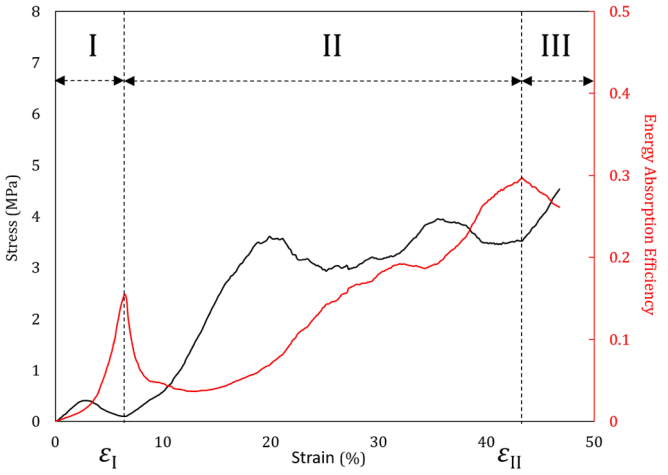

Fig. 11. Schematics of stage division of the stress-strain curve (black) according to the energy absorption efficiency (red). (For interpretation of the references to colour in this figure legend, the reader is referred to the web version of this article.)

they are 42.1 % and 44.7 % lower than the compressive strength of FF (3.8 MPa) is a proof of the impact of the printing direction.

In addition, similar effect is also found in other specimen series ("T" and "L") as well. As seen in Fig. 12, the FF, LL and TT specimens which has the same loading and shell printing directions exhibit higher compressive strength. Particularly, among the tested specimens, the highest compressive strength is 5.61 MPa obtained by the LL specimen while the lowest compressive strength obtained by the LF specimen is 92.4% lower (0.43 MPa), due to the altered printing direction. As can be seen in Fig. 13, the LL exhibit similar deformation process as the FF, therefore strain-hardening behavior is also obtained. In sharp contrast, the LF specimen failed into separate parts early in the stage "I" due to the initiated cracking at the joints, as a result, didn't achieve hardening behavior as indicated by the stress-strain curves in Fig. 8b, and shows low compressive strength. A summary of uniaxial compressive test results is given in Table 4.

As aforementioned, the impact of the printing direction on the compressive strength of the 3D-ACPC is critical. The origin of such impact actually lies in the interface bonding strength of the 3D printed layers. In other words, by enhancing the bonding strength between the printed layers may be an effective method to improve the global mechanical performance of the 3D-ACPC. This can be achieved by optimizing the printing parameters, such as the printing temperature [43] and the cooling speed [44].

3.3. *Deformability and energy absorption*

As shown in the previous section, the FF, LL and TT specimens

Table 4
A summary of uniaxial compressive results, standard deviation is indicated.

Specimen	Compressive strength (MPa)	Deformability (%)	Energy absorption (J)	ε_I (%)	ε_{II} (%)
FF	3.83 ± 0.25	20.01 ± 0.09	63.22 ± 3.64	7.06 ± 0.71	44.16 ± 0.72
FT	2.21 ± 0.43	21.53 ± 0.71	35.83 ± 2.74	5.83 ± 0.42	35.10 ± 1.95
FL	2.10 ± 0.37	22.66 ± 1.79	24.25 ± 3.29	6.31 ± 0.28	38.89 ± 5.71
LL	5.61 ± 0.12	23.47 ± 1.81	77.80 ± 6.11	9.48 ± 0.23	42.96 ± 1.83
LF	0.43 ± 0.05	2.02 ± 0.05	0.61 ± 0.07	5.34 ± 0.99	/
LT	2.18 ± 0.41	18.55 ± 2.15	26.01 ± 1.75	6.39 ± 0.50	36.55 ± 2.55
TT	3.24 ± 0.15	22.34 ± 2.92	50.55 ± 3.44	7.99 ± 1.19	44.96 ± 1.84
TF	2.01 ± 0.23	17.67 ± 1.61	23.40 ± 5.64	6.29 ± 1.07	35.37 ± 2.56
TL	2.58 ± 0.17	23.41 ± 1.63	40.99 ± 4.21	6.10 ± 0.2	35.66 ± 2.33
Mortar cube	35.13 ± 0.17	0.13 ± 0.02	6.37 ± 0.27	/	/
Shell (FF)	0.44 ± 0.13	19.98 ± 1.08	4.62 ± 0.09	/	/
Shell (LL)	0.37 ± 0.08	18.25 ± 0.25	4.74 ± 0.19	/	/
Shell (TT)	0.41 ± 0.05	18.39 ± 0.54	4.46 ± 0.32	/	/

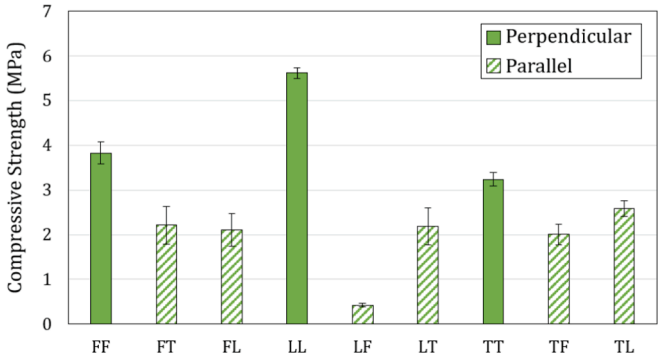

Fig. 12. Compressive strength of the 3D-ACPC categorized by the direcion of the printed interface with respect to the loading direction, standard deviation is indicated.

exhibit higher compressive strength compared to other specimens. In addition, high deformability can be also found in these 3D-ACPC. As seen in Fig. 14, the compressive deformability of FF, LL and TT specimens are 20.0%, 23.5% and 22.3%, respectively. They are significantly higher than the 0.2% deformability of conventional cementitious mortar. Moreover, although similar strain-hardening compressive behavior is also obtained when compressing the printed ABS shell only (shown in Fig. 15), the deformability of the 3D-ACPC is still slightly higher in three different directions.

Owing to such high deformability, these 3D-ACPC exhibit considerably higher energy absorption (defined by the area below the load-displacement curve of the 3D-ACPC excluding stage "III") compared to conventional cementitious mortar. Fig. 15 shows the stress-strain curves of the ABS shell, the overall compressive response of the ABS shell resembles the 3D-ACPC: the ABS shell also shows good deformability. Nevertheless, the compressive strength of the ABS shell is strikingly lower than the 3D-ACPC. As seen in Fig. 15, the second peak of the ABS shell is only approximately 0.5 MPa, even the stress at 45 % of strain is still less than 1 MPa which forms a sharp contrast to the strength of 3D-ACPC. This is a critical drawback of polymeric cellular materials which limit the total energy absorption ability, even they also have excellent deformability. It is shown in Fig. 14 that the absorbed energy of FF, LL and TT reaches 63.2 J, 77.8 J and 50.5 J, respectively. In contrast, the cementitious mortar and the ABS shell are both lower than 10 J. This means that the 3D composites structure simultaneously overcame the low deformability of cementitious mortar and the low energy absorption of ABS shell.

As a cellular material, lightweight is an important feature of the 3D-ACPC. Compared to the density of bulk cementitious mortar (approximately 1850 kg/m^3 for the mixture used in this study), the density of the 3D-ACPC is only 986 kg/m^3. This gives the 3D-ACPC high energy absorption and strength for the same weight. Specially, for the 3D-ACPC developed in this study, the influence of structural anisotropy and shell printing direction is critical. It can be seen in Fig. 16 that the LL specimen shows the highest specific energy absorption 1.23 J/g (absorbed energy per gram of material) and specific strength 5.69 MPa/g·cm^3 (strength divided by density) over all other directions. When compared to the 2D-ACCCs developed in [26,27,45] which was found to have high specific energy absorption, the LL, FF and TT specimens still achieved higher values.

The previous results have already demonstrated the dominative role of the printing process and structural anisotropy on the mechanical properties of the 3D-ACPC. For potential further application of the 3D-ACPC, a proper scale-up strategy is also need to be further addressed. There could be two potential upscale approaches. One is to proportionally enlarge the unit cell, therefore, creating a larger structure from a certain orientation as shown in Fig. 7. The overall mechanical behavior of the upscaled structure should resemble the compressive response of each unit cell elaborated in this study. Of course, the size effect of the constitutive cementitious and polymeric material needs to be considered under. In this case, the influence of printing directions is dominant in the choosing the unit cell. Considering the mechanical performance, the "LL" would easily be an optimal choice if other geometrical parameters in Eq. (1) is still maintained. Another approach would be duplicating the unit cells by multiple times. Then the overall mechanical properties could differ significantly from the individual unit cells. It can be expected that the mechanical performance depends greatly on the spatial arrangement, configuration and total number of the duplicated unit cells, similar to other cellular composites. In this sense, the LL may not necessarily be an optimal choice to create upscaled composites. The second approach is extremely complicated, and the optimization strategy of such composites remains to be investigated in future studies.

4. Conclusions

In the present work, an auxetic cementitious-polymeric composite with architected three-dimensional cellular structure was developed (3D-ACPC). The 3D-ACPC was fabricated by equipping 3D printed polymeric shell with conventional cementitious filler. Compressive behavior of the 3D-ACPC was studied by applying uniaxial compression experiment. Specifically, the deformation behavior, stress-strain response and energy absorption characteristics of the 3D-ACPC were investigated. Based on the obtained experimental results, the following conclusions can be drawn:

- The developed 3D-ACPC shows auxetic behaviour under uniaxial compression (i.e., negative Poisson's ratio) is obtained. The 3D-ACPC achieved a typical three-stage compressive stress-strain response of the auxetic materials.
- Due to the weak interfaces between the 3D printed layers, the influence of the ABS shell printing direction on the properties of 3D-

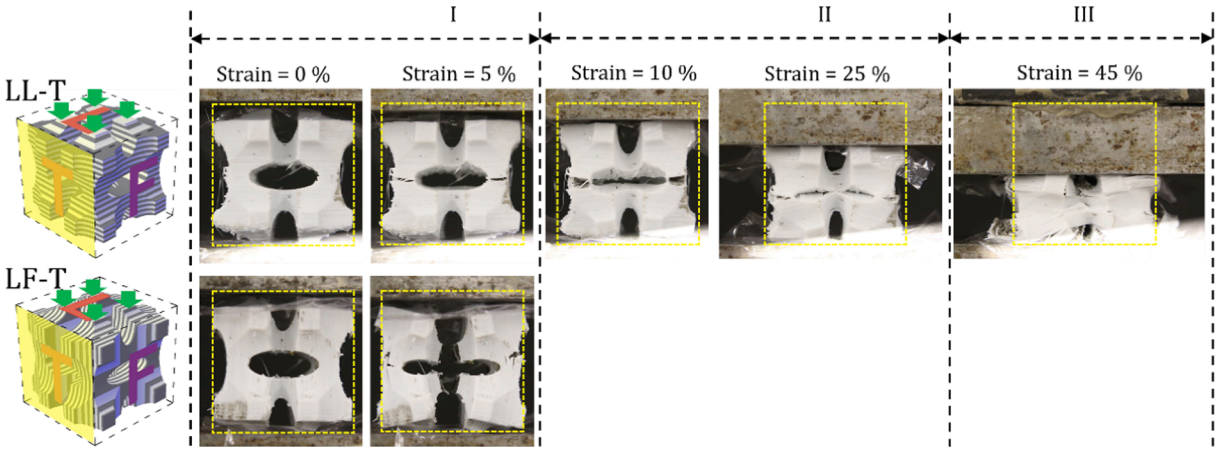

Fig. 13. Deformation process of the LL and LF specimens approximately divided to three stages.

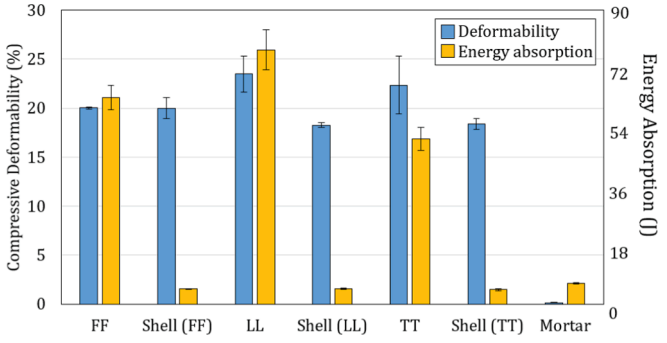

Fig. 14. Energy absorption and deformability of the 3D-ACPC, standard deviation is indicated.

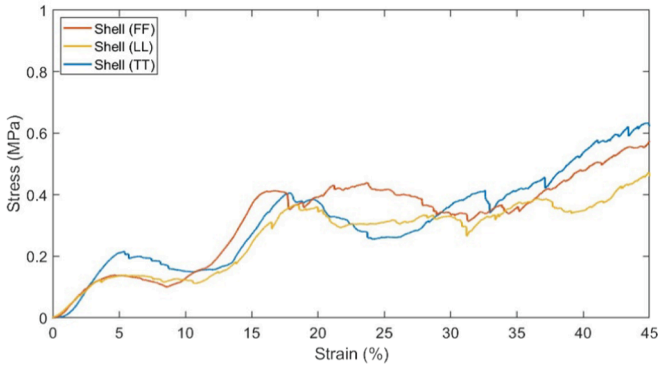

Fig. 15. Stress-strain curves of the ABS shell from different loading directions, note that the Y axis value is significantly lower than the 3D-ACPC in Fig. 8.

ACPC is significant. The compressive strength and energy absorption are strikingly lower when the loading and printing direction is different. The LF specimen (loaded from the "L" direction, printed from the "F" direction) shows 92.33 % and 99.26 % lower compressive strength and energy absorption than the LL specimen (loaded and printed from the "L" direction).

- The 3D-ACPC shows obvious structural anisotropy under uniaxial compression. For specimens with identical loading and shell printing directions, the highest compressive strength and energy absorption is 5.61 MPa and 77.80 J obtained by the LL specimen; while the lowest is 3.24 MPa and 50.55 J obtained by the TT specimen.

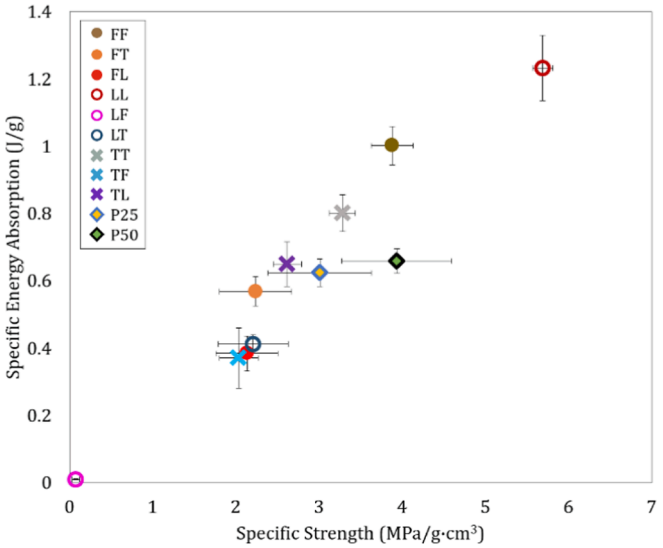

Fig. 16. Specific energy absorption against specific strength of the 3D-ACPC from all nine directions, standard deviation is indicated; data of the P25, P50 is .
adopted from [26,27,45]

- Owing to the 3D cellular composite structure, the 3D-ACPC have overcame the low deformability of sole cementitious mortar and the poor energy absorption ability of sole polymeric shell, therefore, exhibit significantly improved energy absorption ability. The LL specimen achieved 2129 % and 71.21 % higher specific energy absorption than the cementitious mortar and ABS shell, respectively.

The developed 3D-ACPC shows good mechanical properties which gives it great potential to be used in engineering practice. Still, performance of the 3D-ACPC might be further improved by optimizing structural parameters of the 3D cellular structure and tailoring cementitious mixtures. In addition, the 3D-ACPC shows high energy absorption ability under quasi-static load, while the dynamic response of the 3D-ACPC remains to be studied. These aspects are worth of investigating in future work.

CRediT authorship contribution statement

Yading Xu: Conceptualization, Methodology, Data curation, Validation, Formal analysis, Visualization, Writing – original draft, Writing – review & editing. **Branko Šavija:** Writing – review & editing, Project

administration, Supervision, Funding acquisition.

Declaration of Competing Interest

The authors declare that they have no known competing financial interests or personal relationships that could have appeared to influence the work reported in this paper.

Data availability

Data will be made available on request.

Acknowledgements

Yading Xu and Branko Šavija acknowledge the financial support of the European Research Council (ERC) within the framework of the ERC Starting Grant Project "Auxetic Cementitious Composites by 3D printing (ACC-3D)", Grant Agreement Number 101041342.

References

[1] Evans KE. Auxetic polymers: a new range of materials. Endeavour 1991;15(4):170–4.
[2] Hou X, Silberschmidt VV. Metamaterials with Negative Poisson's Ratio: A Review of Mechanical Properties and Deformation Mechanisms; 2015, p. 155-179.
[3] Zhang J, Lu G, You Z. Large deformation and energy absorption of additively manufactured auxetic materials and structures: A review. Compos B Eng 2020;201:108340.
[4] Zhou H, et al. Improving energy absorption capacity of foam concrete with gradient and layered architecture. Constr Build Mater 2022;319.
[5] Rebelo HB, Cismasiu C. Robustness assessment of a deterministically designed sacrificial cladding for structural protection. Eng Struct 2021;240:112279.
[6] Wang Y, et al. Energy absorption performance of a new circular–triangular nested tube and its application as sacrificial cladding. Thin-Walled Struct 2020;157:106992.
[7] Seetoh IP, et al. Extremely stiff and lightweight auxetic metamaterial designs enabled by asymmetric strut cross-sections. Extreme Mech Lett 2022;52.
[8] Jiang F, et al. Quasi-static crushing behavior of novel circular double arrowed auxetic honeycombs: Experimental test and numerical simulation. Thin-Walled Struct 2022;177.
[9] Li C, Shen H-S, Wang H. Postbuckling behavior of sandwich plates with functionally graded auxetic 3D lattice core. Compos Struct 2020;237.
[10] Gao Q, et al. Crashworthiness analysis of double-arrowed auxetic structure under axial impact loading. Mater Des 2019;161:22–34.
[11] Lu Z, et al. Elastic properties of two novel auxetic 3D cellular structures. Int J Solids Struct 2017;124:46–56.
[12] Ren X, et al. Experiments and parametric studies on 3D metallic auxetic metamaterials with tuneable mechanical properties. Smart Mater Struct 2015;24(9):095016.
[13] Zhang X, et al. Quasi-static compression and dynamic crushing behaviors of novel hybrid re-entrant auxetic metamaterials with enhanced energy-absorption. Compos Struct 2022;288.
[14] Shen J, et al. Design and mechanical property studies of 3D re-entrant lattice auxetic structure. Aerosp Sci Technol 2021;118.
[15] Madke RR, Chowdhury R. Anti-impact behavior of auxetic sandwich structure with braided face sheets and 3D re-entrant cores. Compos Struct 2020;236:111838.
[16] Wu W, et al. Mechanical design and multifunctional applications of chiral mechanical metamaterials: A review. Mater Des 2019;180:107950.
[17] Wang Z-P, et al. Integrated shape and size optimization of curved tetra-chiral and anti-tetra-chiral auxetics using isogeometric analysis. Compos Struct 2022;300.
[18] Brendon Francisco M, et al. Multiobjective design optimization of double arrowhead auxetic model using Lichtenberg algorithm based on metamodelling. Structures 2022;45:1199–211.
[19] Lan X-K, et al. Optimal design of a novel cylindrical sandwich panel with double arrow auxetic core under air blast loading. Defence Technology 2020;16(3):617–26.
[20] Airoldi A, et al. Foam-filled energy absorbers with auxetic behaviour for localized impacts. Mater Sci Eng A 2020;788.
[21] Xue Y, Wang W, Han F. Enhanced compressive mechanical properties of aluminum based auxetic lattice structures filled with polymers. Compos B Eng 2019;171:183–91.
[22] Zhao C, et al. Experimental study and finite element analysis on energy absorption of carbon fiber reinforced composite auxetic structures filled with aluminum foam. Compos Struct 2023;303.
[23] Xue Y, et al. Compressive mechanical properties of ex-situ auxetic composite-filled tubes. J Mater Res Technol 2021;14:1644–54.
[24] Asad M, et al. Impact mitigation of masonry walls with carbon fibre and Auxetic fibre composite renders – A numerical study. Structures 2020;28:2733–51.
[25] Li L, et al. 3D face-centered-cubic cement-based hybrid composites reinforced by tension-resistant polymeric truss network. Autom Constr 2020;120:103380.
[26] Xu Y, et al. Cementitious cellular composites with auxetic behavior. Cem Concr Compos 2020;111:103624.
[27] Xu Y, et al. Tunable mechanical behavior of auxetic cementitious cellular composites (CCCs): Experiments and simulations. Constr Build Mater 2021;266:121388.
[28] Xu Y, Šavija B, Schlangen E. Compression Behaviors Of Cementitious Cellular Composites With Negative Poisson's Ratio. FramCos. France; 2019.
[29] Xu Y, Šavija B. Development of strain hardening cementitious composite (SHCC) reinforced with 3D printed polymeric reinforcement: Mechanical properties. Compos B Eng 2019;174:107011.
[30] Xu Y, et al. Cementitious composites reinforced with 3D printed functionally graded polymeric lattice structures: experiments and modelling. Addit Manuf 2021:101887.
[31] Ultimaker, Ultimaker ABS technical data sheet; 2017.
[32] Johnston R, Kazancı Z. Analysis of additively manufactured (3D printed) dual-material auxetic structures under compression. Addit Manuf 2021;38.
[33] Zhang XG, et al. A novel auxetic chiral lattice composite: Experimental and numerical study. Compos Struct 2022;282:115043.
[34] Miltz J, Gruenbaum G. Evaluation of cushioning properties of plastic foams from compressive measurements. Polym Eng Sci 1981;21(15):1010–4.
[35] Wang X, et al. Improving the compressive performance of foam concrete with ceramsite: Experimental and meso-scale numerical investigation. Mater Des 2021;208.
[36] Yang Y, Zhou Q, Deng Y. The reinforcement attributes of multi-scale hybrid fiber throughout the uniaxial compression of ultra-low-weight foamed cement-based composites. Constr Build Mater 2020;242:118184.
[37] Wang B, et al. Investigation of low-velocity impact behaviors of foamed concrete material. Compos B Eng 2019;162:491–9.
[38] Novak N, et al. Blast response study of the sandwich composite panels with 3D chiral auxetic core. Compos Struct 2019;210:167–78.
[39] Van Mier JG. Fracture processes of concrete. CRC Press; 1997.
[40] Wang Y, et al. Strain rate dependent mechanical properties of 3D printed polymer materials using the DLP technique. Addit Manuf 2021;47.
[41] Alharbi N, Osman R, Wismeijer D. Effects of build direction on the mechanical properties of 3D-printed complete coverage interim dental restorations. J Prosthet Dent 2016;115(6):760–7.
[42] Guessasma S, et al. Anisotropic damage inferred to 3D printed polymers using fused deposition modelling and subject to severe compression. Eur Polym J 2016;85:324–40.
[43] Vanaei HR, et al. Toward the understanding of temperature effect on bonding strength, dimensions and geometry of 3D-printed parts. J Mater Sci 2020;55(29):14677–89.
[44] Liu Z, et al. A critical review of fused deposition modeling 3D printing technology in manufacturing polylactic acid parts. Int J Adv Manuf Technol 2019;102(9–12):2877–89.
[45] Xu Y. Architected Cementitious Cellular Materials Towards Auxetic Behavior, in Civil Engineering and Geosciences. TU Delft: Delft, The Netherlands; 2021.